# The driven cavity flow over the whole range of the Knudsen number

Stergios Naris and Dimitris Valougeorgis[a]
*Department of Mechanical and Industrial Engineering, University of Thessaly, Pedion Areos,*
*Volos 38333, Greece*

The flow of a rarefied gas in a rectangular enclosure due to the motion of the upper wall is solved over the whole range of the Knudsen number. The formulation is based on the two–dimensional linearized Bhatnagar-Gross-Krook (BGK) kinetic equation with Maxwell diffuse-specular boundary conditions. The integro-differential equations are solved numerically implementing the discrete velocity method. The discontinuity at the boundaries between stationary and moving walls is treated accordingly. A detailed investigation of the rarefaction effects on the flow pattern and quantities is presented over the whole range of the Knudsen number and various aspect (height/width) ratios. Numerical results of flow characteristics, including the streamlines, the velocity profiles, the pressure and temperature contours, and the drag force of the moving wall, are presented for different aspect ratios and various degrees of gas rarefaction from the free molecular through the transition up to the continuum limit. On several occasions, depending upon the flow parameters, in addition to the main vortex, corner eddies are created. As the depth of the cavity is increased, these eddies grow and merge into additional vortices under the top one. The mesoscale kinetic-type approach proves to be efficient and suitable for problems that incorporate multiscale physics, such as the present nonequilibrium flow. © *2005 American Institute of Physics.* [DOI: 10.1063/1.2047549]

## I. INTRODUCTION

In many instances, fluid flows involved in micro-electrical-mechanical devices, vacuum systems, and high altitude aerodynamics do not have local equilibrium. In these applications, gas flows in channels, tubes, and ducts due to pressure and temperature gradients in the flow direction are very common and have been extensively investigated by solving the hydrodynamic equations with slip boundary conditions[1–3] and by the direct simulation Monte Carlo method.[4,5] In addition, due to the similarity between nonequilibrium flows and rarefied gas flows, corresponding results obtained over the years implementing classical kinetic theory approaches (Boltzmann equation and simplified kinetic models) are also applicable.[6–8]

Another type of flow, which is also encountered in systems not in equilibrium, are boundary driven flows. Prototype flows of this kind are the Couette flow problem in one dimension and the cavity flow problem in two or three dimensions. The Couette flow problem has been studied extensively in Cartesian[9–12] as well as in cylindrical coordinates,[13,14] while the cavity flow problem has received much less attention. It is clarified that in the hydrodynamic limit, the cavity problem is a well known typical benchmark problem for testing and verifying continuum solvers and has been thoroughly studied.[15–17] However, the research work for the same flow pattern in the free molecular, transition, and slip regimes, as far as the authors are aware of, is very limited. Recently, the two-dimensional cavity flow problem was studied using the lattice Boltzmann method[18] with slip boundary conditions. In addition, some results have been

presented for the flow of a gas in a grooved channel using a hydrodynamic approach[19] as well as a kinetic approach.[20] Finally, the gas flow in a square enclosure caused by a discontinuous wall temperature has been studied.[21] The latter is not a boundary driven flow but it is mentioned since the geometrical configuration is similar. Overall, it is noted that the boundary driven flow of a rarefied gas in a cavity, over the whole range of the Knudsen number, which is of particular interest in several fields, has not been thoroughly investigated and more detailed work is needed.

When the flow is close to the continuum regime ($Kn \leqslant 10^{-1}$), the well known hydrodynamic equations coupled with suitable boundary conditions may be applied[19] to yield accurate results for engineering purposes. For $Kn > 10^{-1}$, a kinetic-type approach, based on the Boltzmann equation or on simplified kinetic model equations, is required.[6] It is important to note that the kinetic approach is valid in the whole range of the gas rarefaction. This is an important advantage when systems with multiscale physics are investigated. The well known direct simulation Monte Carlo (DSMC) method[22] is also a powerful computational scheme for $Kn \geqslant 1$. However, for the present flows under investigation, characterized by low Mach and Reynolds numbers, it is difficult to deduce reliable results because the flow is embedded in the statistical noise region and the results are amenable to statistical fluctuations. Instead, the present linearized approach is very suitable for such slow flows. In addition, nowadays, kinetic model equations may be solved by deterministic numerical schemes in a very efficient manner and provide accurate solutions.[23,24]

In the present work, the two-dimensional flow of a gas in a rectangular cavity due to the motion of the upper wall is solved via a kinetic-type approach. The analysis is based on

---

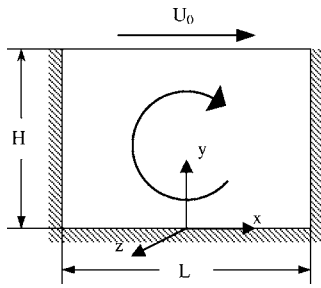[a]Electronic mail: diva@mie.uth.gr

**17**, 097106-1

FIG. 1. Cavity flow configuration.

the linearized Bhatnagar-Gross-Krook (BGK) kinetic equation with Maxwell specular-diffuse boundary conditions. The numerical scheme implements the discrete velocity method, which has been recently applied with great success in single and binary gas flows between plates[25,26] and in orthogonal ducts.[27,28] The corner singularities are treated according to a methodology introduced in Ref. 29. The computational approach is very efficient and accurate and a thorough investigation of the rarefaction effects on the flow pattern is presented over the whole range of the Knudsen number and various aspect (height/width) ratios. Detailed numerical results of the macroscopic flow quantities are provided. Due to the applied linearization, the analysis is valid for small Mach and Reynolds numbers.

## II. FORMULATION OF THE PROBLEM

### A. Flow configuration

A monatomic rarefied gas is contained in a two-dimensional enclosure with rectangular cross section $L \times H$. The orthogonal cross section of the enclosure and the origin of the coordinate system are shown in Fig. 1. The boundaries at $y=0$, $x=-L/2$, and $x=L/2$ are stationary, while the upper boundary at $y=H$ is in motion with a constant horizontal velocity $U_0$. The flow is due to the motion of the lid. All the walls are considered isothermal with a temperature $T_0$. The aspect ratio $A$ of the enclosure is defined by the ratio of the height $H$ over the width $L$ ($A=H/L$), where the width $L$ is taken as the characteristic length of the flow. Thus, the aspect ratio $A$ is equivalent to the nondimensional depth of the cavity. In the present study, we examine the flow characteristics in rectangular cavities with $0.5 < A < 5$. The enclosure is considered as unbounded in the $z$ direction and end effects in that direction are neglected. This flow configuration, shown in Fig. 1, is known as the two-dimensional cavity flow problem.

### B. Basic equations

The original Boltzmann equation, when the BGK model is used for the collision operator and for steady-state flows, takes the form

$$\boldsymbol{\xi} \cdot \frac{\partial f}{\partial \boldsymbol{r}} = \frac{P}{\mu}(f^M - f), \tag{1}$$

where $f=f(\boldsymbol{r}, \boldsymbol{\xi})$ is the unknown distribution function, $\boldsymbol{r}$ is the position vector, $\boldsymbol{\xi}=(\xi_x, \xi_y, \xi_z)$ is the microscopic velocity, $P$

is the local pressure, and $\mu$ is the fluid viscosity at local temperature $T$. Also $f^M$ is the local Maxwellian distribution function given by

$$f^M = \frac{n}{(2\pi RT)^{3/2}} e^{-(\boldsymbol{\xi} - \boldsymbol{V})^2/2RT}, \tag{2}$$

where $R$ is the gas constant defined as the ratio of the Boltzmann constant $k$ over the molecular mass $m(R=k/m)$. The local macroscopic quantities of number density $n$, velocity $\boldsymbol{V}$, and temperature $T$ can be estimated via $f$ as

$$n = \int_{-\infty}^{\infty} f d\boldsymbol{\xi},$$

$$\boldsymbol{V} = \frac{1}{n} \int_{-\infty}^{\infty} \boldsymbol{\xi} f d\boldsymbol{\xi} \quad \text{and} \quad T = \frac{1}{3nR} \int_{-\infty}^{\infty} (\boldsymbol{\xi} - \boldsymbol{V})^2 f d\boldsymbol{\xi}. \tag{3}$$

Other overall quantities of practical interest in the present work are the stress tensor

$$P_{ij} = m \int_{-\infty}^{\infty} (\xi_i - V_i)(\xi_j - V_j) f d\boldsymbol{\xi} \tag{4}$$

and the pressure $P$, which is defined as one-third of the trace of the above tensor and is related to the number density and temperature via the equation of state $P=nkT$.

The equilibrium state is perturbed by the motion of the lid with velocity $U_0 \ll v_0$, where $v_0 = \sqrt{2RT_0}$ is the characteristic molecular velocity. Then, the gas may be considered in a weakly nonequilibrium state and Eq. (1) is linearized by writing the distribution function as

$$f = f^0 \left( 1 + h \frac{U_0}{v_0} \right), \tag{5}$$

where $h=h(\boldsymbol{r}, \boldsymbol{\xi})$ is the unknown perturbed distribution function and

$$f^0 = \frac{n_0}{(2\pi RT_0)^{3/2}} e^{-\xi^2/2RT_0} \tag{6}$$

is the global (absolute) equilibrium distribution function defined at a reference number density $n_0$ and a reference temperature $T_0$. If we expand the local equilibrium distribution function with respect to $f^0$ using the Taylor series and keeping terms up to first order, we get

$$f^M = f^0 \left[ 1 + \varrho + \frac{\boldsymbol{\xi} \cdot \boldsymbol{V}}{RT_0} + \tau \left( \frac{\boldsymbol{\xi}^2}{2RT_0} - \frac{3}{2} \right) \right], \tag{7}$$

where the nondimensional macroscopic quantities are

$$\varrho = \frac{n - n_0}{n_0} \frac{v_0}{U_0} \quad \text{and} \quad \tau = \frac{T - T_0}{T_0} \frac{v_0}{U_0}. \tag{8}$$

Next, by substituting Eqs. (5) and (7) into Eq. (1) we find the linearized BGK equation

$$\boldsymbol{\xi} \cdot \frac{\partial h}{\partial \boldsymbol{r}} = \frac{P_0}{\mu_0}\left[ \varrho + \frac{\boldsymbol{\xi} \cdot \boldsymbol{V}}{RT_0}\frac{v_0}{U_0} + \tau\left(\frac{\xi^2}{2RT_0} - \frac{3}{2}\right) - h\right], \qquad (9)$$

where $P_0$ and $\mu_0$ refer to equilibrium pressure and fluid viscosity at temperature $T_0$, respectively. Finally, defining the nondimensional quantities

$$s = \frac{r}{L}, \quad c = \frac{\xi}{\sqrt{2RT_0}}, \quad \text{and } u = \frac{V}{U_0}, \qquad (10)$$

where $\boldsymbol{s}=(x,y,z)$, $\boldsymbol{c}=(c_x,c_y,c_z)$, and $\boldsymbol{u}=(u_x,u_y,u_z)$, we get the nondimensional kinetic equation

$$\boldsymbol{c} \cdot \frac{\partial h}{\partial \boldsymbol{s}} + \delta h = \delta\left[ \varrho + 2\boldsymbol{c} \cdot \boldsymbol{u} + \tau\left(c^2 - \frac{3}{2}\right)\right], \qquad (11)$$

where

$$\delta = \frac{\sqrt{\pi}}{2}\frac{1}{Kn} = \frac{P_0 L}{\mu_0\sqrt{2RT_0}}. \qquad (12)$$

The parameter $\delta$ is known as the rarefaction parameter and it is proportional to the inverse Knudsen number. The nondimensional macroscopic perturbed quantities of number density, velocity, and temperature are deduced by the moments of $h$ as

$$\varrho = \frac{1}{\pi^{3/2}}\int_{-\infty}^{\infty} h e^{-c^2} d\boldsymbol{c}, \quad \boldsymbol{u} = \frac{1}{\pi^{3/2}}\int_{-\infty}^{\infty} \boldsymbol{c} h e^{-c^2} d\boldsymbol{c}, \quad \text{and}$$

$$(13)$$

$$\tau = \frac{1}{\pi^{3/2}}\int_{-\infty}^{\infty}\left(\frac{2}{3}c^2 - 1\right) h e^{-c^2} d\boldsymbol{c},$$

respectively. In addition, the nondimensional shear stress tensor is given by

$$\Pi_{ij} = \frac{P_{ij}}{2P_0}\frac{v_0}{U_0} = \frac{1}{\pi^{3/2}}\int_{-\infty}^{\infty} c_i c_j h e^{-c^2} d\boldsymbol{c},$$

$$i = x,y,z, \quad j = x,y,z, \quad i \neq j, \qquad (14)$$

while the perturbed nondimensional pressure is

$$p = \frac{P - P_0}{P_0}\frac{v_0}{U_0} = \rho + \tau. \qquad (15)$$

Equation (15) is the linearized equation of state.

We close this subsection by pointing out that in the rest of the paper we are using the rarefaction parameter $\delta$ instead of the Knudsen number.

## C. Reduced kinetic equations after projection

Since the problem under consideration is two-dimensional, the unknown perturbed distribution function in Eq. (11), as well as the overall quantities, do not depend on the $z$ coordinate, i.e., $h(\boldsymbol{s},\boldsymbol{c})=h(x,y,c_x,c_y,c_z)$. Even more, taking advantage of the two-dimensionality of the problem, we can also eliminate the $c_z$ variable by introducing the following projection procedure. First, we multiply Eq. (11) by

$$\frac{1}{\sqrt{\pi}}e^{-c_z^2}$$

and we integrate over all $c_z$. Then, we multiply Eq. (11) for a second time by

$$\frac{1}{\sqrt{\pi}}\left(c_z^2 - \frac{1}{2}\right)e^{c_z^2}$$

and we integrate again over all $c_z$. The resulting equations after the projection are

$$c_x\frac{\partial \phi}{\partial x} + c_y\frac{\partial \phi}{\partial y} + \delta\phi = \delta[\varrho + 2c_x u_x + 2c_y u_y + \tau(c_x^2 + c_y^2 - 1)]$$

$$(16)$$

and

$$c_x\frac{\partial \psi}{\partial x} + c_y\frac{\partial \psi}{\partial y} + \delta\psi = \delta\frac{\tau}{2}, \qquad (17)$$

where the reduced unknown functions $\phi$ and $\psi$ are defined as

$$\phi(x,y,c_x,c_y) = \frac{1}{\sqrt{\pi}}\int_{-\infty}^{\infty} h(x,y,c_x,c_y,c_z)e^{-c_z^2} dc_z \qquad (18)$$

and

$$\psi(x,y,c_x,c_y) = \frac{1}{\sqrt{\pi}}\int_{-\infty}^{\infty} h(x,y,c_x,c_y,c_z)\left(c_z^2 - \frac{1}{2}\right)e^{-c_z^2} dc_z,$$

$$(19)$$

respectively. Equations (16) and (17) are coupled via the macroscopic quantities at the right-hand side of the equations, which now are expressed as

$$\varrho(x,y) = \frac{1}{\pi}\int_{-\infty}^{\infty}\int_{-\infty}^{\infty} \phi e^{-c_x^2 - c_y^2} dc_x dc_y, \qquad (20)$$

$$u_x(x,y) = \frac{1}{\pi}\int_{-\infty}^{\infty}\int_{\infty}^{\infty} \phi c_x e^{-c_x^2 - c_y^2} dc_x dc_y, \qquad (21)$$

$$u_y(x,y) = \frac{1}{\pi}\int_{-\infty}^{\infty}\int_{-\infty}^{\infty} \phi c_y e^{-c_x^2 - c_y^2} dc_x dc_y, \qquad (22)$$

and

$$\tau(x,y) = \frac{1}{\pi}\int_{-\infty}^{\infty}\int_{-\infty}^{\infty}\frac{2}{3}[(c_x^2 + c_y^2 - 1)\phi + \psi]e^{-c_x^2 - c_y^2} dc_x dc_y,$$

$$(23)$$

while

$$\Pi_{xy}(x,y) = \frac{1}{\pi}\int_{-\infty}^{\infty}\int_{-\infty}^{\infty} \phi c_x c_y e^{-c_x^2 - c_y^2} dc_x dc_y. \qquad (24)$$

The elimination of one (or more) component of the particle velocity by a projection procedure, when allowed by the flow configuration, is quite important for the computational efficiency of the numerical scheme. It is obvious that in the case of the three-dimensional cavity problem, a projection of the present type without missing important features of the

flow is not possible and then the solution should be based on Eq. (11) instead of Eqs. (16) and (17). It is noted that, although the boundaries of the cavity are at isothermal conditions, we have included the temperature variation in the formulation due to compressibility effects. It turns out, as discussed later, that in this flow configuration the temperature variation is small and may be neglected, but in general this cannot be taken for granted. In addition, the analysis is more accurate and more easily extended to nonisothermal cavity flow. In any case, if the temperature perturbation is assumed equal to zero, then the projection defined by Eq. (19) can be omitted and the whole formulation is simplified.

For computational purposes, it is more convenient to express the two components of the particle velocity in polar coordinates, while the spatial variables are kept in a Cartesian coordinate system. By defining the new dimensionless polar variables $0 \leq \mu < \infty$ and $0 \leq \theta \leq 2\pi$ as

$$\mu = \sqrt{c_x^2 + c_y^2} \quad \text{and} \quad \theta = \arctan(c_y/c_x), \tag{25}$$

the coupled equations (16) and (17) are rewritten as

$$\mu\left[\cos\theta\frac{\partial\phi}{\partial x} + \sin\theta\frac{\partial\phi}{\partial y}\right] + \delta\phi$$
$$= \delta[\varrho + 2\mu(u_x\cos\theta + u_y\sin\theta) + \tau(\mu^2 - 1)] \tag{26}$$

and

$$\mu\left[\cos\theta\frac{\partial\psi}{\partial x} + \sin\theta\frac{\partial\psi}{\partial y}\right] + \delta\psi = \delta\frac{\tau}{2}. \tag{27}$$

Finally, the nondimensional macroscopic quantities given by Eqs. (20)–(24) are now expressed as

$$\varrho(x,y) = \frac{1}{\pi}\int_0^{2\pi}\int_0^\infty \phi\mu e^{-\mu^2}d\mu d\theta, \tag{28}$$

$$u_x(x,y) = \frac{1}{\pi}\int_0^{2\pi}\int_0^\infty \phi\mu^2 e^{-\mu^2}\cos\theta d\mu d\theta, \tag{29}$$

$$u_y(x,y) = \frac{1}{\pi}\int_0^{2\pi}\int_0^\infty \phi\mu^2 e^{-\mu^2}\sin\theta d\mu d\theta, \tag{30}$$

$$\tau(x,y) = \frac{1}{\pi}\int_0^{2\pi}\int_0^\infty \frac{2}{3}[(\mu^2-1)\phi + \psi]\mu e^{-\mu^2}d\mu d\theta, \tag{31}$$

and

$$\Pi_{xy}(x,y) = \frac{1}{\pi}\int_0^{2\pi}\int_0^\infty \phi\mu^3 e^{-\mu^2}\sin\theta\cos\theta d\mu d\theta. \tag{32}$$

The introduced linear transformation from $(c_x, c_y)$ into $(\mu, \theta)$ contains certain computational advantages in terms of the discretization approach. The kinetic equations (26) and (27) together with the integral expressions (28)–(31) form a closed set of integro-differential equations. The boundary conditions of this set are discussed in the next section.

## D. Boundary conditions

On the boundaries, the distribution function of leaving particles $(f^+)$ is expressed by the Maxwell-type diffuse boundary condition[6]

$$f^+ = f_w^{eq}, \tag{33}$$

where

$$f_w^{eq} = \frac{n_w}{(2\pi RT_w)^{3/2}}e^{-(\xi - U_w)^2} \tag{34}$$

is the local Maxwellian distribution defined by the velocity $U_w$ and temperature $T_w$ of the wall, while $n_w$ is a parameter, which ensures the impermeability condition at the wall.

Applying the linearization procedure and introducing the nondimensional variables of Sec. II B, it is easily found that

$$h^+ = \varrho_w + 2\mathbf{c}\cdot\frac{\mathbf{U_w}}{U_0} + \tau_w\left(c^2 - \frac{3}{2}\right), \tag{35}$$

where $\mathbf{U_w}/U_0$ and $\tau_w$ denote the nondimensional velocity vector and temperature, respectively, of the boundary. The nondimensional quantity $\varrho_w$ can be estimated by the usual impermeability condition, which states that the normal component of the gas velocity on the wall vanishes.[6] Next, the projection procedure as well as the mapping in the polar coordinate system $(\mu, \theta)$, applied in Sec. II C, reduce the boundary condition (35) to

$$\phi^+ = \varrho_w + 2\mu\left(\cos\theta\frac{(U_w)_x}{U_0} + \sin\theta\frac{(U_w)_y}{U_0}\right) + \tau_w(\mu^2 - 1) \tag{36}$$

and

$$\psi^+ = \frac{1}{2}\tau_w. \tag{37}$$

Again, the superscript + denotes leaving distributions, while $(U_w)_x$ and $(U_w)_y$ correspond to the $x$ and $y$ components of the boundary velocity. Finally, taking into account that the three walls of the cavity are stationary and that the lid is moving in the $x$ direction with velocity $U_0$, as well as that all four walls are at isothermal conditions $(\tau_w = 0)$, yields at the three stationary walls

$$\phi(x, 0, \mu, \theta) = \rho_w(x, 0), \quad \psi(x, 0, \mu, \theta) = 0 \quad \text{for } 0 < \theta < \pi, \tag{38}$$

$$\phi\left(-\frac{1}{2}, y, \mu, \theta\right) = \rho_w\left(-\frac{1}{2}, y\right), \tag{39}$$

$$\psi\left(-\frac{1}{2}, y, \mu, \theta\right) = 0 \quad \text{for } -\frac{\pi}{2} < \theta < \frac{\pi}{2},$$

$$\phi\left(\frac{1}{2}, y, \mu, \theta\right) = \rho_w\left(\frac{1}{2}, y\right), \tag{40}$$

$$\psi\left(\frac{1}{2}, y, \mu, \theta\right) = 0 \quad \text{for } \frac{\pi}{2} < \theta < \frac{3\pi}{2}$$

and at the moving wall $(y = A = H/L)$

$$\phi(x,A,\mu,\theta) = \rho_w(x,A) + 2\mu \cos \theta,$$

$$\psi(x,A,\mu,\theta) = 0 \quad \text{for } \pi < \theta < 2\pi. \tag{41}$$

The parameter $\varrho_w$ at the four walls is estimated by applying the impermeability condition at each boundary to find

$$\varrho_w(x,0) = -\frac{2}{\sqrt{\pi}}\int_\pi^{2\pi}\int_0^\infty \phi(x,0,\mu,\theta)\mu^2 e^{-\mu^2}\sin\theta d\mu d\theta, \tag{42}$$

$$\varrho_w\left(-\frac{1}{2},y\right) = -\frac{2}{\sqrt{\pi}}\int_{\pi/2}^{3\pi/2}\int_0^\infty \phi\left(-\frac{1}{2},y,\mu,\theta\right)\mu^2 e^{-\mu^2}$$
$$\times \cos\theta d\mu d\theta, \tag{43}$$

$$\varrho_w\left(\frac{1}{2},y\right) = \frac{2}{\sqrt{\pi}}\int_\pi^{2\pi}\int_0^\infty \phi\left(\frac{1}{2},y,\mu,\theta\right)\mu^2 e^{-\mu^2}\cos\theta d\mu d\theta, \tag{44}$$

and

$$\varrho_w(x,A) = \frac{2}{\sqrt{\pi}}\int_0^\pi\int_0^\infty \phi(x,A,\mu,\theta)\mu^2 e^{-\mu^2}\sin\theta d\mu d\theta. \tag{45}$$

Thus, the governing equations (26) and (27) are subject to the boundary conditions (38)–(41), supplemented by the conditions (42)–(45).

## III. TREATMENT OF THE BOUNDARY-INDUCED DISCONTINUITY

The propagation of boundary-induced discontinuities in the distribution function of kinetic and transport model equations has been studied in several contributions.[30,29] Due to the propagating discontinuities, the overall space-dependent quantities suffer from unphysical oscillatory behavior. This is a numerical problem caused by finite difference approximations across the discontinuities; in the area of neutron and radiative transfer, they are known as "ray effects."[31] By increasing the number of discretization points in the phase space, the problem is treated partially because, although the amplitude of the oscillations is decreased, their frequency is increased. A more efficient way to treat the discontinuities, which is adapted in the present work, is to apply a methodology proposed in Ref. 29 for the one-speed transport equation in a half-space. The main idea is based on the fact that in the estimation of the discontinuities coming from the boundaries, the scattering term in the kinetic equation can be neglected.

In the present flow, the discontinuities exist at the four corners, where the distribution function $\phi$ is required to be bivalued [see boundary conditions (38)–(41) for $\phi$]. These discontinuities in the boundary conditions propagate through the numerical solution of Eq. (26) inside the computational domain and result in density, velocity, pressure, and temperature profiles with nonphysical oscillations. Most of the numerical problems are caused by the singularities at the top

two corners of the cavity due to the strong discontinuities in the velocity between stationary and moving walls. As is expected, these numerical problems become more severe as the rarefaction parameter is decreased (i.e., as we are approaching the free molecular regime). It is noted that these problems do not exist in the numerical solution of Eq. (27), since the associated boundary conditions (38)–(41) for $\psi$ are homogeneous and equal to zero.

To demonstrate the treatment of the boundary-induced discontinuities in $\phi$, we rewrite Eq. (26) in the more compact form

$$D\phi + \delta\phi = \delta I, \tag{46}$$

where

$$D = \mu\left[\cos\theta\frac{\partial}{\partial x} + \sin\theta\frac{\partial}{\partial y}\right] = -\mu\frac{\partial}{\partial s} \tag{47}$$

denotes the differential operator acting on $\phi$, while $s$ is the characteristic direction and

$$I = \varrho + 2\mu(u_x\cos\theta + u_y\sin\theta) + \tau(\mu^2 - 1). \tag{48}$$

Following Ref. 29, we decompose $\phi$ into two parts, namely

$$\phi = \phi_1 + \phi_2. \tag{49}$$

Equation (49) is substituted into Eq. (46) and the associated boundary conditions (38)–(41) to yield two subproblems. The first one is for $\phi_1$, described by the differential equation

$$D\phi_1 + \delta\phi_1 = 0 \tag{50}$$

with $\phi_1^+ = 0$ at the three stationary walls and $\phi_1^+ = 2\mu\cos\theta$ at the moving wall (the $+$ denotes outgoing flux). This problem is solved analytically by integrating along the characteristics to yield

$$\phi_1(x,y,\mu,\theta) = \phi_1^+ e^{-\delta s_0/\mu}, \tag{51}$$

where $s_0$ is the distance along the characteristic line between the point $(x,y)$ and the corresponding boundary point. The second subproblem is for $\phi_2$, described by the integro-differential equation

$$D\phi_2 + \delta\phi_2 = \delta I \tag{52}$$

with $\phi_2^+ = \rho_w$ at the four boundaries, while $\rho_w$ is the prescribed parameter of the gas at the corresponding wall, given by Eqs. (42)–(45). Thus, the strong discontinuity due to the lid motion has been removed. The transport equations for $\phi_2$ and $\psi$ are solved numerically in an iterative manner, according to the discretization scheme described in the next section, while the analytical solution for $\phi_1$ is estimated once and it is valid throughout the iterative process. At each iteration step, the overall quantities are estimated using $\phi_1$, $\phi_2$, and $\psi$.

Following the above procedure, supplemented by a reasonably dense grid and an adequately large set of discrete velocities, we are able to eliminate completely the oscillations of the macroscopic profiles.
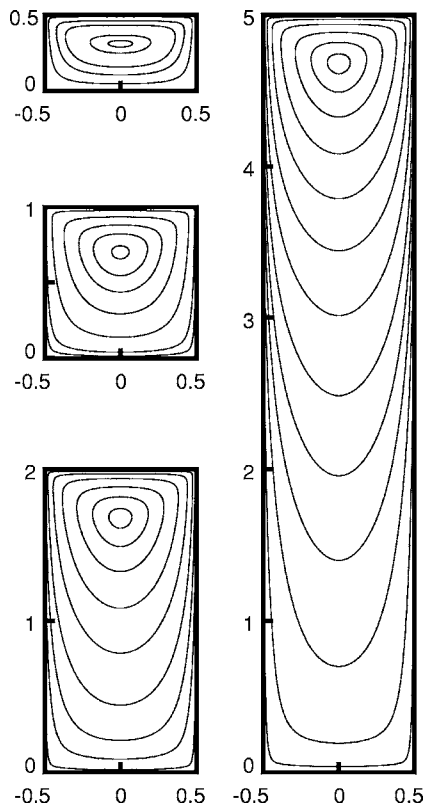
FIG. 2. Velocity streamlines for $\delta=1$ and $A=0.5,1,2,5$.
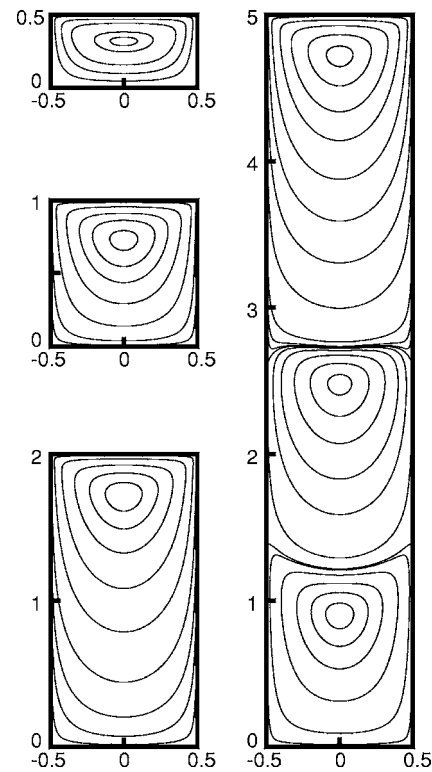


FIG. 3. Velocity streamlines for $\delta=5$ and $A=0.5,1,2,5$.

## IV. THE NUMERICAL SCHEME

The coupled integro-differential equations (26) and (27), supplemented by the integral expressions (28)–(31) of the overall quantities and the associated boundary conditions (38)–(41), are solved numerically in an iterative manner. The discretization in the physical and particle velocity spaces is based on typical second-order finite difference schemes[31] and the discrete velocity method for steady-state equations,[7] respectively.

The discretization in the physical space $(x,y)$ is performed by dividing the flow domain in rectangular elements, denoted by $(i\times j)$, with $i=1,2,\ldots,I$ and $j=1,2,\ldots,J$. The first derivatives in $x$ and $y$ are approximated by centered finite differences in the corresponding direction and then all terms are interpolated in terms of the corresponding quantities at the edges of each element using weighted averages. The scheme is known as the weighted diamond difference scheme and the spatial discretization is second order accurate.[31]

In the particle velocity space, the discretization is performed by choosing a suitable set of discrete velocities $(\mu_m,\theta_n)$, defined by $0\leq\mu_m<\infty$ and $0\leq\theta_n\leq2\pi$, with $m=1,2,\ldots,M$ and $n=1,2,\ldots,N$. The resulting set consists of $M\times N$ discrete velocities.

Based on the above-described discretization, the unknown functions $\phi(x,y,\mu,\theta)$ and $\psi(x,y,\mu,\theta)$ described by the integro-differential equations (26) and (27) are substituted by the discretized $\phi_{i,j,m,n}$ and $\psi_{i,j,m,n}$ approximated by a set of algebraic equations. Thus, there are $2\times M\times N$ equations for each of the $I\times J$ elements. The quantities on the

right-hand sides of Eqs. (26) and (27) are estimated using the corresponding summation formulas

$$\varrho_{i,j}=\frac{1}{\pi}\sum_{n=1}^{N}\sum_{m=1}^{M}w_m\phi_{i,j,m,n}\mu_m e^{-\mu_m^2}\Delta\theta, \tag{53}$$

$$(u_x)_{i,j}=\frac{1}{\pi}\sum_{n=1}^{N}\sum_{m=1}^{M}w_m\phi_{i,j,m,n}\mu_m^2 e^{-\mu_m^2}\cos\theta_n\Delta\theta, \tag{54}$$

$$(u_y)_{i,j}=\frac{1}{\pi}\sum_{n=1}^{N}\sum_{m=1}^{M}w_m\phi_{i,j,m,n}\mu_m^2 e^{-\mu_m^2}\sin\theta_n\Delta\theta, \tag{55}$$

and

$$\tau_{i,j}=\frac{1}{\pi}\sum_{n=1}^{N}\sum_{m=1}^{M}\frac{2}{3}w_m[(\mu_m^2-1)\phi_{i,j,m,n}+\psi_{i,j,m,n}]\mu_m e^{-\mu_m^2}\Delta\theta, \tag{56}$$

where $\mu_m$ and $w_m$ are the roots and the corresponding weights of a suitable Gauss quadrature defined on the integration interval $[0,\infty)$, while $\Delta\theta=2\pi/N$. In a similar manner, we find

$$\Pi_{i,j}=\frac{1}{\pi}\sum_{n=1}^{N}\sum_{m=1}^{M}w_m\phi_{i,j,m,n}\mu_m^3 e^{-\mu_m^2}\sin\theta_n\cos\theta_n\Delta\theta. \tag{57}$$

The discretized version of Eqs. (26) and (27) and the associated summations (53)–(56) are solved in an iterative manner. The iterative procedure is ended when the imposed convergence criterion on the overall quantities is satisfied. At each iteration step, the solution is achieved by a marching
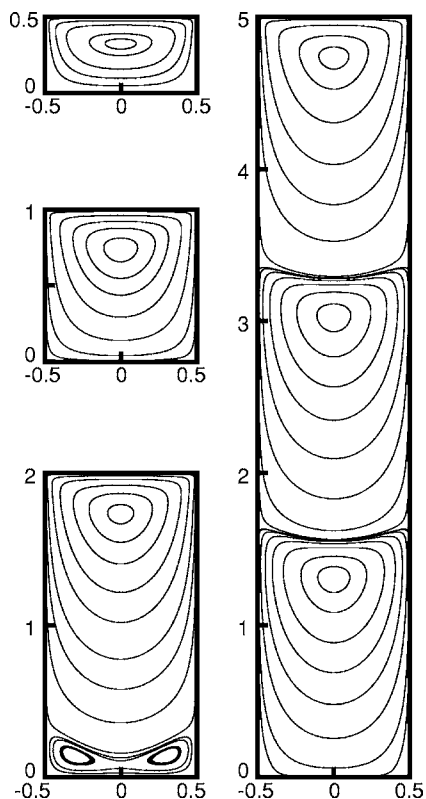
FIG. 4. Velocity streamlines for $\delta=10$ and $A=0.5,1,2,5$.
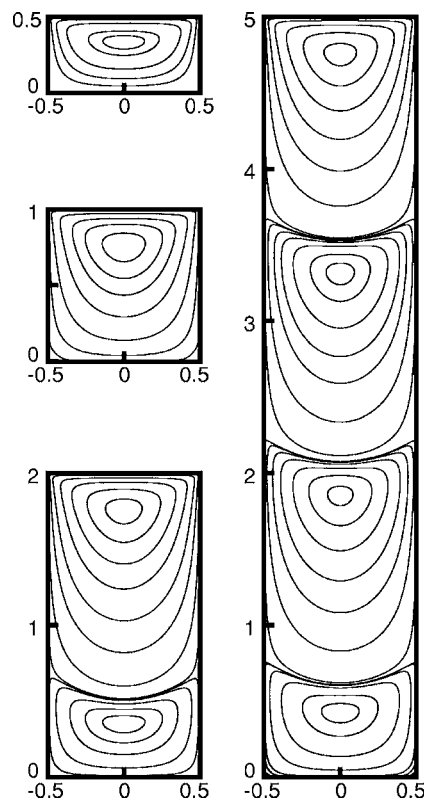


FIG. 5. Velocity streamlines for $\delta=100$ and $A=0.5,1,2,5$.

scheme. For each discrete velocity $(\mu_m, \theta_n)$, the distribution functions at each node are computed explicitly marching through the physical domain. Following this procedure, no matrix inversion is required.

## V. RESULTS AND DISCUSSION

It is important to recall that due to the linearized analysis, the results are valid for small Mach and Reynolds numbers. Taking into account the relation $Re \sim \delta Ma$, the above restriction implies that for $\delta \leqslant 1$, the condition $U_0/v_0 \ll 1$ is adequate, while for $\delta > 1$, the required condition becomes $\delta U_0/v_0 \ll 1$.

The calculations have been carried out over a wide range of the rarefaction parameter and various values of the aspect ratio. In particular, results are presented for $\delta = 10^{-3}, 10^{-2}, 10^{-1}, 1, 5, 10, 10^2$ and $A=0.5, 1, 2, 5$. Depending on the geometrical configuration, the absolute convergence criteria in the calculations are between $10^{-11}$ and $10^{-14}$. The discretization in the phase space (physical and molecular velocity spaces) has been progressively refined to ensure accurate results up to several significant figures. In general, in rarefied atmospheres we need a large number of discrete velocities, while the physical grid may be coarse. On the other hand, in continuum atmospheres the required number of discrete velocities may be reduced, but dense physical grids are important to achieve good accuracy. The presented results are with $h_x=h_y=10^{-2}$ for all $\delta$ and $A$, while the number of discrete velocities $M \times N$ is $64 \times 400$ for $\delta \leqslant 1$, $16 \times 400$ for $\delta > 1$, and $16 \times 40$ for $\delta = 10^2$.

Figures 2–5 show plots of the velocity streamlines for $\delta=1, 5, 10,$ and $10^2$, respectively, and in each figure results are provided for various values of depth $A$. The flow is always symmetric about $x=0$. Starting with $\delta=1$ in Fig. 2, a general idea of the flow pattern with respect to $A$ is given and in all cases a single vortex is created. The corresponding velocity streamlines for $\delta=5$ are given in Fig. 3. It is seen that while for $A=0.5$, 1, and 2 there is only one vortex, for $A=5$ two additional vortices, under the first one, have been developed. The mechanism that creates these additional vortices is more clearly demonstrated in Figs. 4 and 5, where the velocity streamlines for $\delta=10$ and $10^2$ are shown, respectively. It is seen in Fig. 4 that, for $A=2$, under the main vortex secondary eddies have been created at the two bottom corners. As the depth $A$ is increased further, these secondary eddies grow and merge into a second vortex under the first one. In the same figure, it is seen that for $A=5$, based on this mechanism, two new vortices under the first one have been developed. In Fig. 5, for $\delta=10^2$, there are two vortices for $A=2$ and four vortices for $A=5$. It may be deduced that for each $\delta$ there is a critical value of $A$ above which corner eddies are initiated, and as the depth $A$ is increased further, these corner eddies result in new counter-rotating vortices. This process is repeated as the depth is increased. The rarefaction effect on the flow patterns can be easily realized by comparing in Figs. 2–5 the streamlines with the same $A$. It is clearly demonstrated that as the rarefaction parameter $\delta$ is decreased (i.e., as the rarefaction of the gas is increased) and we are approaching the free molecular limit, the critical depth $A$, above which the first corner eddies show up, is increased.

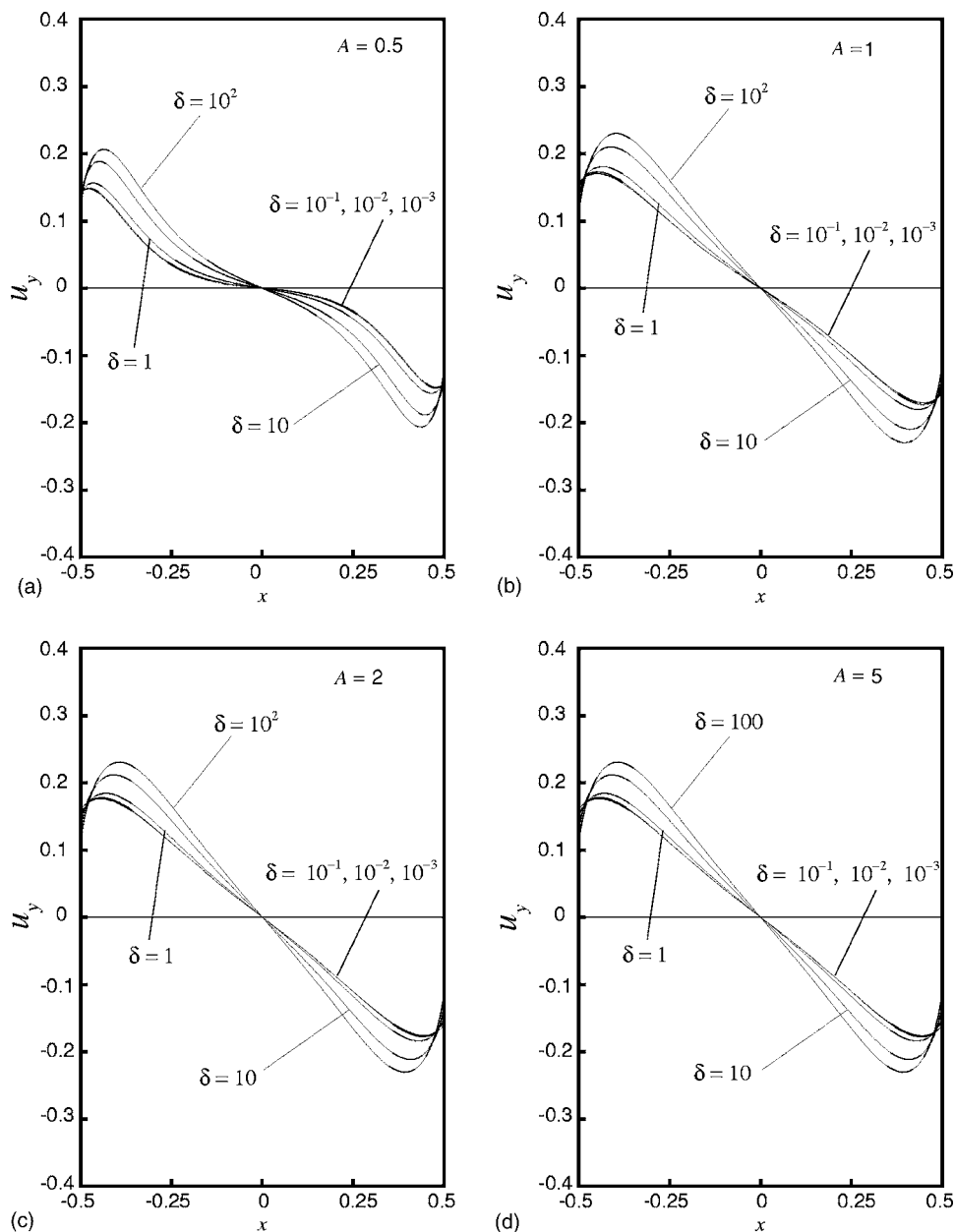It is interesting to note that in a recent review article[17] on

FIG. 6. Profiles of the vertical component of the velocity on a horizontal plane crossing the center of the top vortex, for various values of $\delta$ and $A$.

the classical continuum cavity problem, a very similar mechanism of eddy creation was reported at the Stokes limit ($Re=0$). The present results in Fig. 5, for $\delta=10^2$, which is close to the continuum limit, have an excellent qualitative resemblance with the results reported in Ref. 17 This supports the expected accuracy of the implemented kinetic approach, since the corresponding results in Ref. 17 are analytical. It is clarified that the analytical results in Ref. 17 are at the continuum limit for the Reynolds number equal to zero, while the present results in Fig. 5 are for flow conditions close to the continuum limit and for small Reynolds numbers.

Having a clear qualitative picture of the flow patterns for various $\delta$ and $A$, we turn our attention to some quantitative results. The vertical velocities on a horizontal plane crossing the center of the top vortex are shown in Fig. 6 for all values

of $\delta$ and $A$ under investigation. The shape of the profiles in the shallow cavity, with $A=0.5$, is different compared to the corresponding shapes in the other configurations, with $A=1$, 2, and 5, which are similar to each other. Also, the effect of the rarefaction $\delta$ on the velocity profiles and on the velocity slip at the boundary may be observed. The results for $\delta=10^{-3}$, $10^{-2}$, and $10^{-1}$ are very close and therefore they are represented by a single line. Next, in Figs. 7(a) and 7(b), the vertical velocities on the horizontal planes crossing the center of the second and third vortices are shown, respectively, for $A=5$ and $\delta=5$, 10, and $10^2$. By examining these results as well as the corresponding results of Fig.6(d), it is concluded that the maximum absolute values of the vertical velocities between the first (top), second, and third (bottom) vortices are reduced by several orders of magnitude. This result is general. For all cases tested, the maximum absolute veloci-
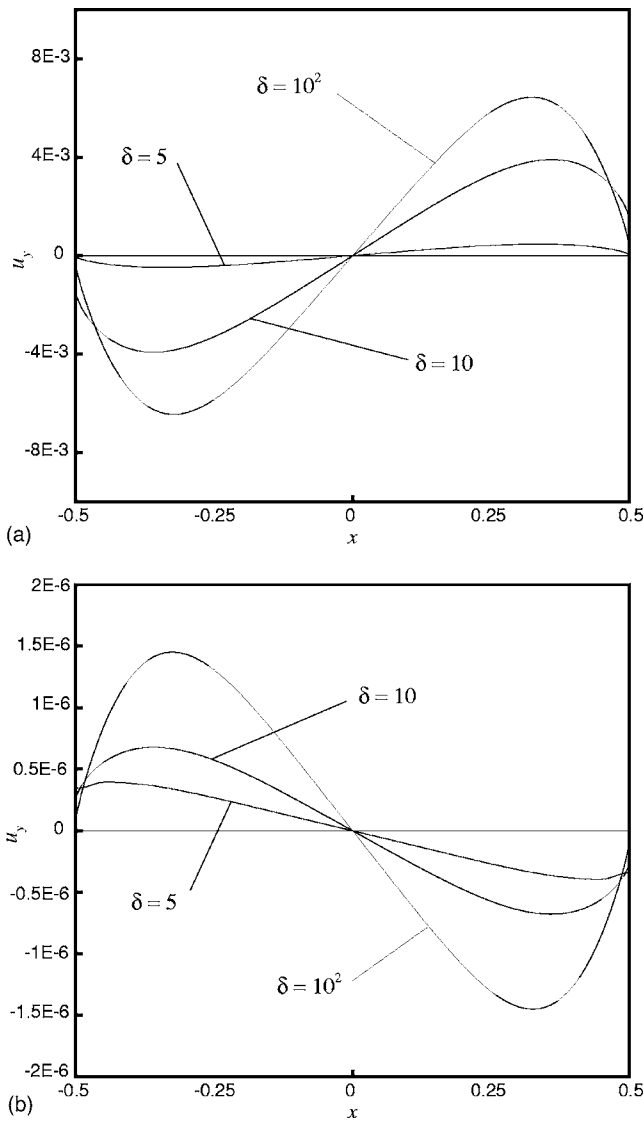
FIG. 7. Profiles of the vertical component of the velocity on a horizontal plane crossing the center of the second (a) and third (b) vortices, for $A=5$ and various values of $\delta$.

ties between adjacent (well developed) vortices, as we are moving from top to bottom, are reduced by two to three orders of magnitude.

The horizontal velocities on a plane crossing the center of the cavity are shown in Fig. 8 for $\delta=10^{-2}, 1, 10^2$, and all $A$ under investigation. Across this plane, the vertical velocities are zero. In most cases, there is one vortex in the cavity and the velocity profiles cross the axis $x=0$ only once. However, for $\delta=10^2$ there are two vortices when $A=2$ and four vortices when $A=5$ (see also Fig. 5). This is not readily observed in Fig. 8 since, as mentioned before, the magnitude of the velocities from the top eddy to the next ones is rapidly reduced. For that reason, in Fig. 8 and for $\delta=10^2$, enlarged details of segments of the velocity profiles at certain locations along the $y$ axis have been provided using the appropriate scales. It is obvious that the points at which the velocity profiles cross the axis $x=0$ are the centers of the counter-rotating vortices.

In Fig. 9, we show the relative vertical distance $(y/A)$ of the center of the top vortex from the bottom of the cavity in
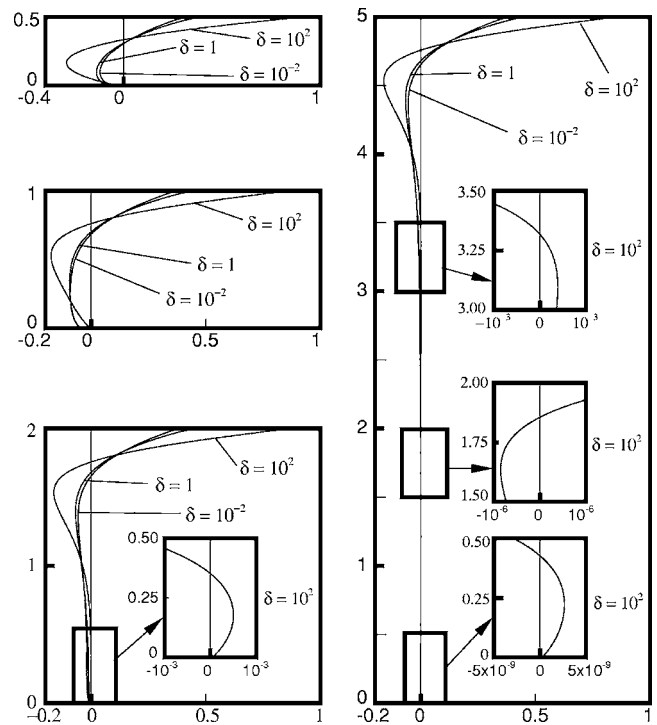


FIG. 8. Profiles of the horizontal component of the velocity on a vertical plane crossing the center of the cavity, for various values of $\delta$ and $A$.

terms of $\delta$ for $A=0.5$, 1, 2, and 5. The flow is symmetric about $x=0$, so the center of the primary vortices is always at $x=0$. It is seen that in all cases, as $\delta$ is increased, the center of the top vortex is moved slightly toward the moving wall. These plots are presented in terms of the relative vertical distance in order to distinguish the results between the various depths. Actually, the absolute distance of the center of the top vortex for a given $\delta$ remains almost unchanged for $A \geqslant 1$. Even more, the structure of the existing vortices is not modified as $A$ is increased and new vortices under the exist-
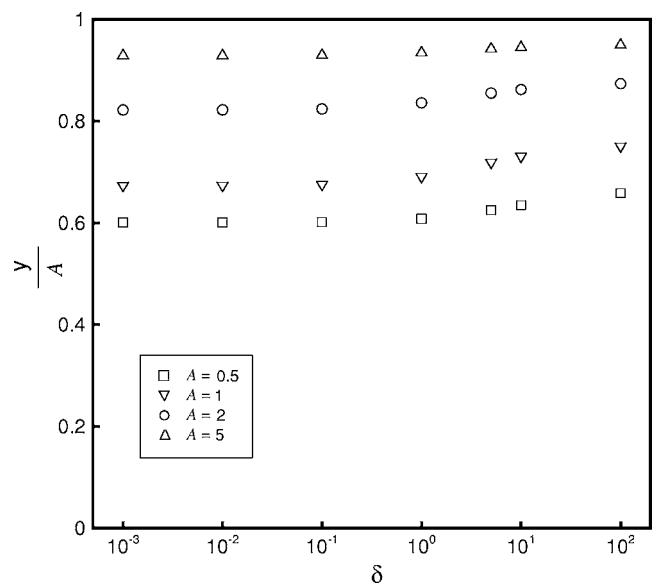


FIG. 9. Location of the center of the top vortex for various values of $\delta$ and $A$.

TABLE I. Reduced flow rate between the center of the top vortex and the moving plate for various values of $\delta$ and $A$.

| | Reduced flow rate | | | |
|---|---|---|---|---|
| $\delta$ | $A=0.5$ | $A=1$ | $A=2$ | $A=5$ |
| $10^{-3}$ | 0.53 (−1) | 0.97 (−1) | 0.10 | 0.10 |
| $10^{-2}$ | 0.53(−1) | 0.97(−1) | 0.10 | 0.10 |
| $10^{-1}$ | 0.54(−1) | 0.97(−1) | 0.10 | 0.10 |
| 1 | 0.62(−1) | 0.10 | 0.11 | 0.11 |
| 5 | 0.84(−1) | 0.13 | 0.13 | 0.13 |
| 10 | 0.99(−1) | 0.14 | 0.15 | 0.15 |
| $10^2$ | 0.14 | 0.18 | 0.18 | 0.18 |

ing ones are created. The only effect is that, during this process, the existing eddies are pushed slightly upward. The velocity profiles shown in Figs. 6–8 support this argument.

In Table I, we present the reduced flow rate between the moving wall of the cavity and the center of the top vortex for various values of $\delta$ and $A$. These results are obtained by integrating the velocity profile, given by Eq. (29), along this distance. It is seen that for a given $\delta$, the flow rate is increased with increasing $A$ and finally it reaches a constant value. This is expected, since the flow structure and characteristics of the top vortex do not alter above some value of $A$, even if the depth is increased further. The exact estimate of this value of $A$ depends on $\delta$ but it is seen that in all cases it is about $A=2$. It is also seen that for a given $A$, the reduced flow rate remains almost constant for $10^{-3} \leqslant \delta \leqslant 10^{-1}$, then for $1 \leqslant \delta \leqslant 50$ it is linearly increased proportionally to the logarithm of $\delta$, and finally it reaches the continuum limit about $\delta=10^2$.

The drag coefficient of the top moving wall is obtained by integrating the reduced shear stress, given by Eq. (32), along the lid of the cavity. The results are presented in Table II for various values of $\delta$ and $A$. The reduced shear stress and consequently the drag coefficient always decrease by increasing $\delta$. This is in agreement with corresponding results for the Couette flow problem in single gases and mixtures.[32] For large $\delta$, the values of the drag coefficient are close to the corresponding ones, obtained by implementing Newton's lin-

TABLE II. Drag coefficient of the moving wall for various values of $\delta$ and $A$.

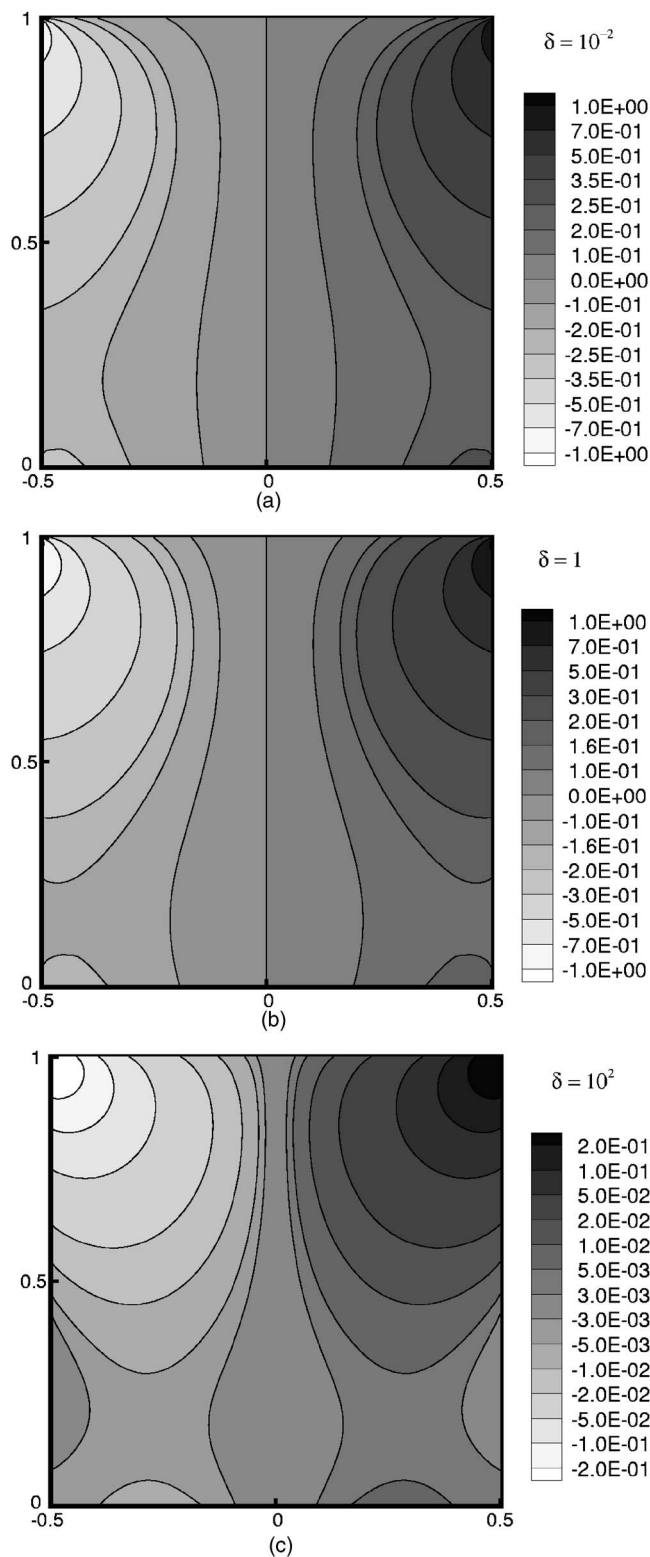| | Drag coefficient | | | |
|---|---|---|---|---|
| $\delta$ | $A=0.5$ | $A=1$ | $A=2$ | $A=5$ |
| $10^{-3}$ | 0.73 | 0.69 | 0.67 | 0.67 |
| $10^{-2}$ | 0.73 | 0.68 | 0.67 | 0.67 |
| $10^{-1}$ | 0.73 | 0.68 | 0.67 | 0.67 |
| 1 | 0.68 | 0.63 | 0.63 | 0.63 |
| 5 | 0.55 | 0.51 | 0.51 | 0.51 |
| 10 | 0.45 | 0.42 | 0.42 | 0.42 |
| $10^2$ | 0.15 | 0.16 | 0.16 | 0.16 |



FIG. 10. Pressure contours for $A=1$ and various values of $\delta$.

ear constitutive relation between stress and strain. The drag coefficient is decreased as $A$ is increased and finally it reaches (not surprisingly) a constant value.

Typical pressure and temperature contours for $A=1$ and $\delta=10^{-2}, 1, 10^2$ are shown in Figs. 10 and 11, respectively. All perturbation profiles are antisymmetric about $x=0$, where they vanish. In addition to the pressure and temperature per-
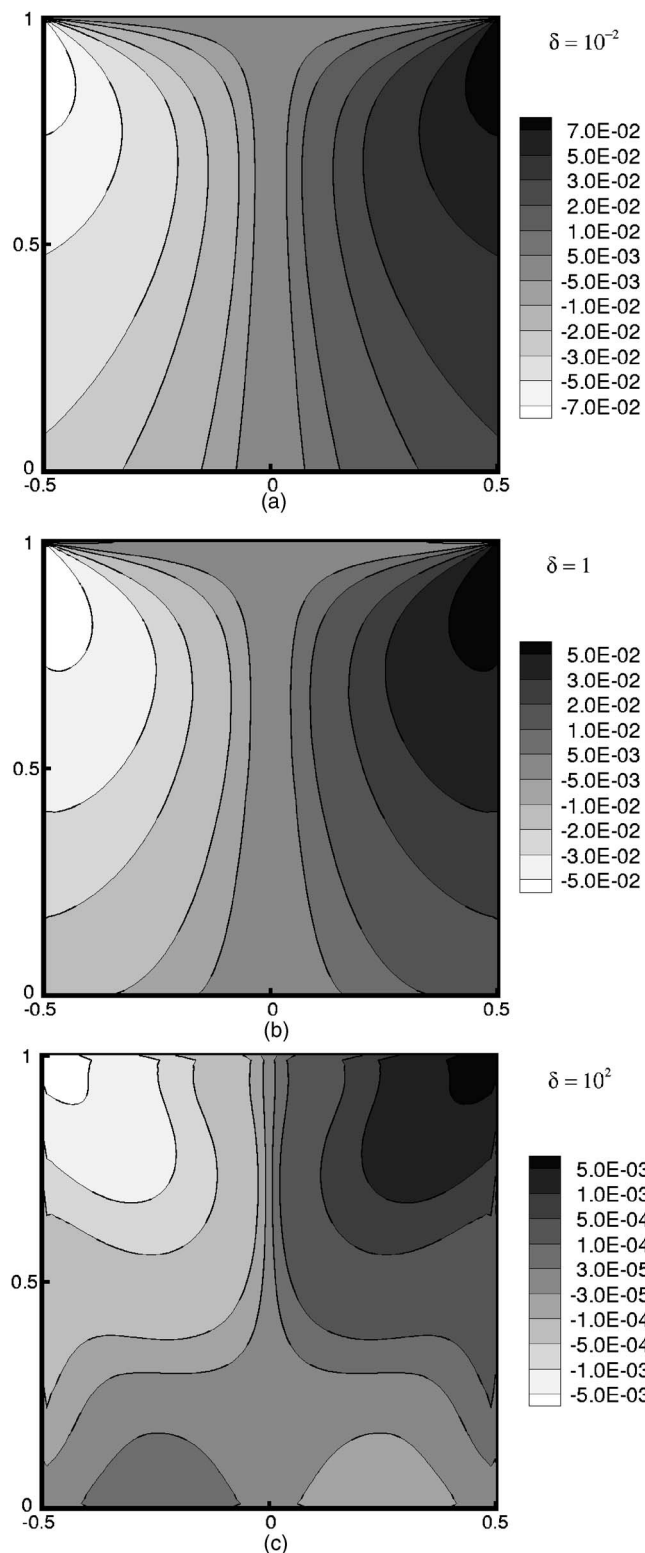
$\delta = 10^{-2}$

7.0E-02
5.0E-02
3.0E-02
2.0E-02
1.0E-02
5.0E-03
-5.0E-03
-1.0E-02
-2.0E-02
-3.0E-02
-5.0E-02
-7.0E-02

(a)

$\delta = 1$

5.0E-02
3.0E-02
2.0E-02
1.0E-02
5.0E-03
-5.0E-03
-1.0E-02
-2.0E-02
-3.0E-02
-5.0E-02

(b)

$\delta = 10^2$

5.0E-03
1.0E-03
5.0E-04
1.0E-04
3.0E-05
-3.0E-05
-1.0E-04
-5.0E-04
-1.0E-03
-5.0E-03

(c)

FIG. 11. Temperature contours for $A=1$ and various values of $\delta$.

turbations, the number density profiles have also been estimated via the distribution function, and in all cases the linearized equation of state has been verified. It is deduced that the pressure and density perturbations have the same order, while the temperature variation is smaller by at least one order of magnitude and could be neglected. Also, as $\delta$ is increased and we are moving from the free molecular to the continuum regime, the perturbations in density, pressure, and temperature are reduced. These results are indicative and similar behavior has been observed for other values of $\delta$ and $A$.

## VI. CONCLUDING REMARKS

The flow of a rarefied gas in a rectangular cavity due to the driven upper wall is studied over the whole range of the rarefaction parameter $\delta$ and various depths $A$. The formulation is based on the two-dimensional linearized BGK kinetic equation, and the resulting integro-differential equations are solved numerically implementing the discrete velocity method. A detailed investigation of the rarefaction effects on the flow pattern and quantities is presented. It has been found that as the depth of the cavity is increased, corner eddies are created that grow and merge and finally result in new counter-rotating vortices. During this process, the existing vortices are pushed slightly upward, while their structure and flow characteristics remain almost unchanged. It is also demonstrated that as $\delta$ is decreased, the critical $A$, above which the first corner eddies show up, is increased. The results, which are based on kinetic theory, recover properly the hydrodynamic solution at the continuum limit. The mesoscale kinetic-type approach proves to be quite efficient and suitable for problems that incorporate multiscale physics, such as the present nonequilibrium flow.

## ACKNOWLEDGMENTS

[1] C. M. Ho and Y. C. Tai, "Micro-electro-mechanical systems (MEMS) and fluid flows," Annu. Rev. Fluid Mech. **30**, 579 (1998).
[2] A. Beskok and G. E. Karniadakis, "A model for flows in channels, pipes, and ducts at micro and nano scales," Microscale Thermophys. Eng. **3**, 43 (1999).
[3] D. Jie, X. Diao, K. B. Cheong, and L. K. Yong, "Navier-Stokes simulations of gas flow in micro devices," J. Micromech. Microeng. **10**, 372 (2000).
[4] E. P. Muntz, "Rarefied gas dynamics," Annu. Rev. Fluid Mech. **21**, 387 (1998).
[5] E. S. Oran, C. K. Oh, and B. Z. Cybyk, "Direct simulation Monte Carlo: Recent advances and applications," Annu. Rev. Fluid Mech. **30**, 403 (1998).
[6] C. Cercignan, *The Boltzmann Equation and Its Application* (Springer, New York, 1988).
[7] F. Sharipov and V. Seleznev, "Data on internal rarefied gas flows," J. Phys. Chem. Ref. Data **27**, 657 (1998).
[8] C. Cercignani, *Rarefied Gas Dynamics. From Basic Concepts to Actual Calculations* (Cambridge University Press, Cambridge, 2000).
[9] D. R. Willis, "Comparison of kinetic theory analyses of linearized Couette flow," Phys. Fluids **5**, 127 (1962).
[10] C. Cercignani and C. D. Pagani, "Variational approach to boundary value problems in kinetic theory," Phys. Fluids **9**, 1167 (1966).
[11] C. Cercignani and S. Cortese, "Validation of a Monte Carlo simulation of the plane Couette flow of a rarefied gas," J. Stat. Phys. **75**, 817 (1994).
[12] W. Marques, Jr., G. M. Kremer, and F. M. Sharipov, "Couette flow with slip and jump boundary conditions," Continuum Mech. Thermodyn. **16**, 379 (2000).
[13] K. Nanbu, "Analysis of cylindrical Couette flows by use of the direction simulation method," Phys. Fluids **27**, 2632 (1984).

[14] F. M. Sharipov and G. M. Kremer, "Non-isothermal Couette flow of a rarefied gas between two cylinders," Eur. J. Mech. B/Fluids **18**, 121 (1999).

[15] S. P. Vanka, "Block-implicit multigrid solution of Navier-Stokes equations in primitive variables," J. Comput. Phys. **65**, 138 (1986).

[16] S. Hou, Q. Zou, S. Chen, and G. Doolen, "Simulation of cavity flow by the lattice Boltzmann method," J. Comput. Phys. **118**, 329 (1995).

[17] P. N. Shankar and M. D. Deshpande, "Fluid mechanics in the driven cavity," Annu. Rev. Fluid Mech. **32**, 93 (2000).

[18] H. Nie, G. Doolen, and S. Chen, "Lattice Boltzmann simulations of fluid flows in MEMS," J. Stat. Phys. **112**, 279 (2002).

[19] G. E. Karniadakis and A. Beskok, *Micro Flows. Fundamentals and Simulation* (Springer, New York, 2001).

[20] K. Yamamoto, H. Takeuchi, and T. Hyakutake, "Effect of surface grooves on the rarefied gas flow between two parallel walls," in *Proceedings of the 24th Conference on Rarefied Gas Dynamics*, Monopoli (Bari), Italy 10-16 July 2004, edited by M. Capitelli, Vol. 762, pp. 156–161.

[21] K. Aoki, S. Takata, and H. Aikawa, "A rarefied gas flow caused by a discontinuous wall temperature," Phys. Fluids **13**, 2645 (2001).

[22] G. A. Bird, *Molecular Gas Dynamics and the Direct Simulation of Gas Flows* (Oxford University Press, Oxford, 1994).

[23] F. M. Sharipov and E. A. Subbotin, "On optimization of the discrete velocity method used in rarefied gas dynamics," ZAMP **44**, 572 (1993).

[24] D. Valougeorgis and S. Naris, "Acceleration schemes of the discrete velocity method: Gaseous flows in rectangular microchannels," SIAM J. Sci. Comput. (USA) **25**, 534 (2003).

[25] C. E. Siewert and D. Valougeorgis, "The McCormack model: Channel flow of a binary gas mixture driven by temperature, pressure and concentration gradients," Eur. J. Mech. B/Fluids **23**, 645 (2004).

[26] S. Naris, D. Valougeorgis, D. Kalempa, and F. Sharipov, "Gaseous mixture flow between two parallel plates in the whole range of the gas rarefaction," Physica A **336**, 294 (2004).

[27] S. Naris, D. Valougeorgis, F. Sharipov, and D. Kalempa, "Discrete velocity modelling of gaseous mixture flows in MEMS," Superlattices Microstruct. **35**, 629 (2004).

[28] S. Naris, D. Valougeorgis, D. Kalempa, and F. Sharipov, "Flow of gaseous mixtures through rectangular microchannels driven by pressure, temperature and concentration gradients," Phys. Fluids **17** (2005).

[29] K. Aoki, C. Bardos, C. Dogbe, and F. Golse, "A note on the propagation of boundary induced discontinuities in kinetic theory," Math. Models Meth. Appl. Sci. **11**, 1581 (2001).

[30] Y. Sone and T. Takata, "Discontinuity of the velocity distribution function in a rarefied gas around a convex body and the s layer at the bottom of the Knudsen layer," Transp. Theory Stat. Phys. **21**, 501 (1992).

[31] E. E. Lewis and W. F. Miller, Jr., *Computational Methods in Neutron Transport Theory* (Wiley, New York, 1984).

[32] F. Sharipov, L. M. G. Cumin, and D. Kalempa, "Plane Couette flow of binary gaseous mixture in the whole range of the Knudsen number," Eur. J. Mech. B/Fluids **23**, 899 (2004).